Research Square

Preprints are preliminary reports that have not undergone peer review.
They should not be considered conclusive, used to inform clinical practice,
or referenced by the media as validated information.

Numerical Back-Analysis of Eccentrically Loaded Circular Footings on Geonet-Reinforced Sand

SeyedMahmood Ghassemizadeh

sg4044@hw.ac.uk

Heriot-Watt University

Asifur Rahman Abir

Heriot-Watt University

Amin Mazaherizaveh

Royal Roads University

Research Article

Keywords: Geonet, Circular footing, Eccentric loading, Finite element back-analysis, Settlement definition, Loss of contact

Posted Date: November 25th, 2026

DOI: https://doi.org/10.21203/rs.3.rs-11759751/v1

License: This work is licensed under a Creative Commons Attribution 4.0 International License.
Read Full License

Additional Declarations: No competing interests reported.

Numerical Back-Analysis of Eccentrically Loaded Circular Footings on Geonet-Reinforced Sand

Abstract

Model tests on eccentrically loaded footings on reinforced sand record load, settlement and tilt, but not the reinforcement tension or the contact area. This study back-analyses 25 published model tests on a rigid circular footing (D = 300 mm) on dense sand with one geonet layer. The geonet diameter was 1–4.5D, and the eccentricity was up to D/4. Axisymmetric and three-dimensional Abaqus/Explicit models were first checked against exact solutions. The Mohr–Coulomb sand parameters were calibrated on the unreinforced test under central load only. The other 24 tests were computed without further adjustment. Under central load, the computed bearing capacity ratio of the largest geonet differed from the test by 1–4 % at 5 % and 10 % settlement, within the calibration uncertainty. Under eccentric load, the comparison depended strongly on the settlement definition, which the original study does not report. With the settlement of the loaded edge, the root-mean-square error fell from 61–148 % (centre) to 7–31 %, and a kinematic check of the published data supports this reading. Outside the kern, the peak-based bearing capacity ratio was reproduced within −7 % to +4 %. Most geonet tension developed within one diameter of the footing centre, consistent with the small gain beyond a geonet diameter of 2D. The rotation line derived from two transducers did not coincide with the edge of contact. The model under-predicted the geonet benefit at small tilt and over-predicted the unreinforced eccentric response; both limitations are quantified.

Keywords: Geonet; Circular footing; Eccentric loading; Finite element back-analysis; Settlement definition; Loss of contact

1 Introduction

Shallow foundations often carry a moment as well as a vertical load. Wind, earth pressure and machine loads are common sources of this moment. The moment can be expressed as a vertical load acting at an eccentricity e. Eccentricity reduces the bearing capacity and makes the footing

tilt [1, 2]. Under a large eccentricity, part of the footing base also separates from the soil. Geosynthetic reinforcement is widely used to raise the bearing capacity of footings on sand and to reduce their settlement [3–6]. Most of this knowledge, however, comes from tests and analyses with a central load. Under an eccentric load, the reinforcement works below a tilted footing with a non-uniform and partly lost contact. How the reinforcement then carries load, and how its size affects this, is less well understood.

Model tests on reinforced sand under eccentric load have mainly used strip footings [7–9]. For circular footings, Badakhshan and Noorzad [10] tested a 120 mm footing on sand with one to four geogrid layers. In their tests, the bearing capacity ratio increased with eccentricity up to the kern boundary and decreased beyond it. Later studies compared circular and square footings under similar conditions [11, 12]. Recent tests have also examined skirted or reinforced circular footings under eccentric load [13, 14]. These tests give load–settlement curves and, in some cases, the tilt. They do not give the tension in the reinforcement, the contact pressure or the size of the contact area. The mechanisms behind the measured trends are therefore inferred rather than observed.

Numerical analyses can supply these quantities. For eccentric and inclined loads on reinforced soil, most numerical studies have used limit analysis of strip footings [15–18]. Limit analysis gives the collapse load, but not the settlement, the tilt or the loss of contact. Numerical studies of reinforced circular and ring footings have mostly considered a central load, with limit analysis [19] or with displacement-based finite elements [20, 21]. Badakhshan and Noorzad [11] combined model tests with numerical analyses of circular and square footings under central and eccentric load, and reported close agreement between the computed and measured load–settlement curves. In such studies, the models are usually compared with the same tests that were used to set their parameters. Their predictive ability is then difficult to judge [22]. In addition, the measured settlement of an eccentrically loaded footing depends on where it is measured, and practice differs between studies (Section 6.1).

Dastpak et al. [23], hereafter referred to as the source, reported 25 model tests on a rigid circular footing with a diameter of 300 mm. The footing rested on dense sand with one geonet layer. The geonet diameter was one to 4.5 times the footing diameter, and the eccentricity was up to one quarter of the diameter. The tests raised three questions that the measurements alone cannot answer. First, the bearing capacity ratio increased with eccentricity, also outside the kern. This differs from the trend reported by Badakhshan and Noorzad [10]. Second, the benefit of the geonet grew strongly up to a diameter of twice the footing diameter, but much less beyond it. Third, a rotation line derived from two displacement transducers suggested loss of contact even on the kern boundary. The tests recorded only the load and two displacements, and the source does not state which settlement is plotted for the eccentric tests. To the authors' knowledge, these tests have not been analysed numerically.

This study presents a numerical back-analysis of the complete test series of the source with axisymmetric and three-dimensional finite element models. It differs from earlier numerical work in four respects. (i) The sand parameters are calibrated on a single test, the unreinforced footing under central load, and the other 24 tests are computed without further adjustment. The test data were published before this study, so these are not Class A predictions in the sense of Lambe [24]; nevertheless, the fixed parameters allow the predictive ability of the model to be assessed. (ii) The settlement definition with which the eccentric test curves are consistent is identified, both with the model and with a model-independent kinematic check of the published data. (iii) The rotation line derived from two transducers is compared with the true contact edge computed from the contact pressure. (iv) The geonet tension is used to examine why the benefit grows with eccentricity and why it changes little beyond a geonet diameter of 2D. The published data are digitised from the source and checked for internal consistency, the models are verified against exact solutions, and the limitations of a Mohr–Coulomb model with a perfectly bonded geonet are quantified.

2 Reference Tests and Data

2.1 Test set-up

The tests were carried out in a steel tank with a diameter of 1.4 m and a height of 0.9 m [23]. The same tank and curtain pluviation system were used in earlier studies of the same laboratory; the pluviation system produced uniform specimens over a wide range of relative density [25]. The laboratory later examined the effect of perforated plates on the relative density of pluviated sands [26]. The footing was a rigid aluminium plate with a diameter D of 300 mm and a thickness of 30 mm, with a layer of sand glued to its base. The load was applied by a load-controlled hydraulic jack at 20 N/s, through a ball-and-socket joint, and measured by a load cell. Two displacement transducers (LVDTs) on the two sides of the footing measured settlement and tilt; their exact positions are not given. In one series, a third transducer confirmed that the footing did not rotate in the perpendicular plane. The sand was a poorly graded silica sand (Table 1), pluviated to a relative density of 72 %. This corresponds to a dry unit weight of 15.03 kN/m³. The reinforcement was one layer of HDPE geonet at a depth u of 50 mm (u/D = 0.17). This depth followed earlier tests in the same tank, in which the bearing capacity of a 300 mm footing decreased as the geogrid depth increased from 0.17D to D [27]. The source states that the geonet has equal tensile strength in all directions.

Five series were tested: unreinforced (UR) and reinforced with D_g/D = 1, 2, 3 and 4.5, where D_g is the geonet diameter. Each series had five eccentricities, e/D = 0, 0.0625, 0.125, 0.1875 and 0.25. At least one test of each series was repeated (seven repeats in total). The kern of a circular footing has a radius of D/8, so the last two eccentricities lie outside it. The source took the ultimate load by tangent intersection [28] on or inside the kern and as the peak load outside it.

Table 1 Test programme and material properties [23]

Item	Value
Tank diameter × height	1.4 m × 0.9 m
Footing	rigid aluminium, D = 300 mm, t = 30 mm, rough base

Sand	poorly graded silica sand; D10/D30/D50/D60 = 0.48/0.62/0.67/0.71 mm; Cu = 1.48; Cc = 1.13; Gs = 2.65
Unit weight	γmin = 13 kN/m³, γmax = 16 kN/m³; Dr = 72 % (γd = 15.03 kN/m³)
Geonet	HDPE; aperture 6 × 8 mm; 730 g/m²; thickness 3.3 mm
Geonet stiffness and strength	axial stiffness 179 kN/m at 2 % and 104 kN/m at 5 % strain; Tult = 5.7 kN/m at 9 %
Geonet depth	u = 50 mm (u/D = 0.17)
Variables	Dg/D = 0 (UR), 1, 2, 3, 4.5; e/D = 0, 0.0625, 0.125, 0.1875, 0.25 (25 tests)

2.2 Extraction and consistency of the published data

Only the published figures were available. Fig. 2 (load–settlement curves of the UR and D_g/D = 4.5 series) and Fig. 7 (rotation line) of the source are vector graphics. They were read directly from the drawing paths of the PDF file. The reading error is smaller than the drawn line width, about 0.5 kPa and 0.04 % in *S/D*. Figs. 3 and 4 of the source and its plot of the bearing capacity ratio against tilt (the tilt plot) are raster images with known abscissae. Their ordinates were found from the marker centres, with an uncertainty of about ±0.015 where markers overlap. The abscissa of the tilt plot is the tilt in units of 10^{-2} rad.

Two checks were made before the data were used. First, the legend of the three dashed UR curves in Fig. 2 of the source appears to be permuted. Taken at face value, it gives peak pressures of 56, 107 and 82 kPa for *e/D* = 0.0625, 0.125 and 0.1875. This order is not monotonic, and it disagrees with Fig. 5 and the text of the source. The curves with peaks of 107, 82 and 56 kPa were therefore assigned to *e/D* = 0.0625, 0.125 and 0.1875. With this assignment, the bearing capacity ratios computed from Fig. 2 of the source agree with its Fig. 4 within 0.01–0.02 for *e/D* = 0.0625, 0.125 and 0.25. The peaks outside the kern then give Q_u/Q_0 = 0.44 and 0.28 and BCR_u = 2.16 and 2.45, against 0.44, 0.27, 2.162 and 2.470 in the source. Second, some differences remain. For *e/D* = 0, Fig. 2 of the source gives BCR_s = 1.06–1.23 at *S/D* = 1–5 %, whereas its Fig. 4 shows 1.01–1.09. The tangent windows used inside the kern are not given, and fixed windows did not reproduce the published values. The comparisons therefore rely mainly on full curves, on BCR_s at fixed settlement and on peak-based values outside the kern. These quantities are defined in the same way for the tests and the model.

3 Numerical Model

3.1 Models and meshes

All analyses were carried out with Abaqus/Explicit 2025 as quasi-static analyses. An implicit solution was tried first. It needed artificial stabilisation and failed to converge at small settlement, where the sand at the footing edge has almost no confinement. Two models were used (Fig. 1). An axisymmetric model served for verification, calibration and the central-load computations. A three-dimensional half model served for all eccentricities. Both models represent the full tank, 1.4 m in diameter and 0.9 m deep (Fig. 1a). The axisymmetric sand mesh had four-node reduced-integration elements (CAX4R). The base mesh had 7560 elements, with 5 mm elements below and next to the footing. All reinforced axisymmetric analyses used a mesh with element sizes reduced by 25 % (13 447 elements, 3.75 mm at the footing; Fig. 1b); the reason is given in Section 4.2. The half model had 36 400 eight-node reduced-integration elements (C3D8R), with 10 mm elements at the footing edge (Fig. 1c). Both meshes had nodal lines at the four geonet radii and at the geonet depth, so that the same mesh could be used for every geonet size. The input files were generated, and the results extracted, with Python scripts written for this study with the assistance of a generative AI tool (see Declarations). The scripts were checked through the verification analyses of Section 4.

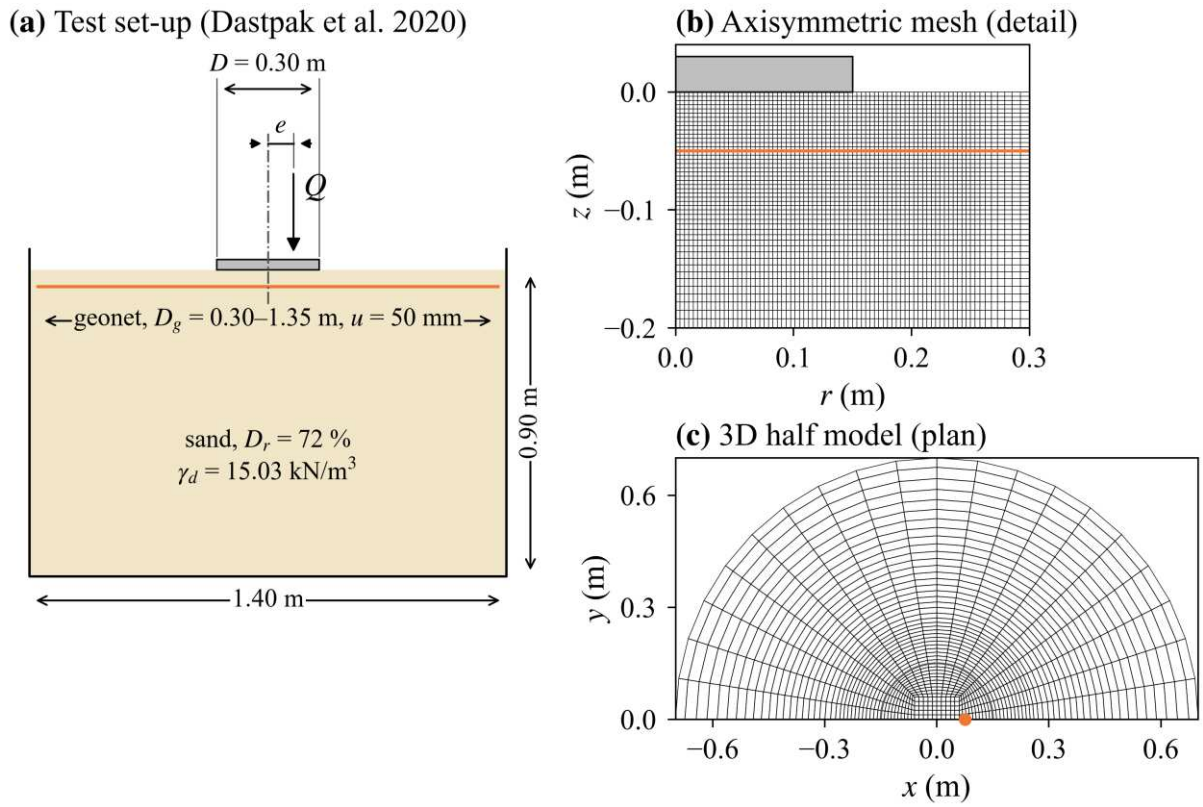

Fig. 1 Test set-up and numerical models: (a) test set-up; (b) axisymmetric mesh near the footing; (c) three-dimensional half model in plan

3.2 Sand and geonet

The sand was modelled as a linear elastic, perfectly plastic Mohr–Coulomb material with non-associated flow (Table 2). The friction angle φ, the dilation angle ψ and Young's modulus E were calibrated on one test (Section 5.1). The modulus is an operative value for a model test at low stress. A cohesion of 0.02 kPa was used for numerical reasons only; it adds about 2 % to the capacity. The initial horizontal stress was set with $K_0 = 1 - \sin \varphi_{cv} = 0.455$, with an assumed critical-state angle φ_{cv} of 33°.

The geonet was modelled as a membrane with a thickness of 3.3 mm. The half model used four-node membrane elements (M3D4R). Abaqus/Explicit has no axisymmetric membrane, so the axisymmetric model used two-node shell elements (SAX1) of negligible bending stiffness. The geonet shared its nodes with the sand, so no slip was allowed. An isotropic material with a Poisson's ratio of 0.30 was used, because the product has equal strength in all directions. The two axial stiffness values of Table 1 were interpreted as secant values, which gives T(2 %) = 3.58 kN/m and T(5 %) = 5.20 kN/m. The tension–strain curve $T = \varepsilon/(a + b\varepsilon)$ was fitted exactly

through these two points. This gives $a = 2.901 \times 10^{-3}$ m/kN, $b = 0.1343$ m/kN and an initial stiffness of 345 kN/m. Beyond 5 %, the tension rises linearly to 5.7 kN/m at 9 % and then stays constant. The curve was entered as an elastic–plastic material with von Mises yielding. Under biaxial tension, the major principal tension can then exceed the uniaxial value by up to $2/\sqrt{3}$, that is, 15 %. Rupture was not modelled in the main analyses; its effect is examined in Section 7.3. Mass scaling was applied to the geonet elements only, so that they did not control the stable time increment.

Table 2 Model parameters

Component	Parameter	Value	Source
Sand	ρ	1532 kg/m³	γd of the tests
	E, ν	4.0 MPa, 0.30	E calibrated; ν assumed
	φ, ψ, c	38°, 5°, 0.02 kPa	φ, ψ calibrated; c numerical
	K0	0.455 (φ_{cv} = 33°)	assumed
Geonet	t, ν	3.3 mm, 0.30	Table 1; assumed
	T(ε)	ε/(a + bε) to 5 %, linear to 5.7 kN/m at 9 %, then constant	fitted to Table 1
	interface	perfect bond	assumed
Footing	base contact	μ = 0.65 (≈ tan φ_{cv}), hard, separation allowed	assumed
	load point	30 mm above the base at x = e; vertical displacement prescribed; horizontal displacement and rotation free	test set-up
Boundaries	wall / base	smooth / fixed	tank

3.3 Footing, loading and output

The footing was a rigid body with frictional contact on the sand. The base friction coefficient was 0.65, close to tan φ_{cv}, because sand was glued to the base. The contact allowed separation. The load was applied through a reference node at the ball joint, 30 mm above the base and at a distance e from the centre (Fig. 1c). Its vertical displacement was prescribed. Its horizontal displacement and rotation were free, so the load stayed vertical and the joint transmitted no moment. The first three-dimensional analyses had the horizontal displacement fixed. They developed a horizontal force of up to 31 % of the vertical force, which is an inclined load, not the vertical eccentric load of the tests. The boundary condition was therefore changed after this

first comparison. The change lowered the unreinforced peak at e/D = 0.25 from 47.1 to 40.0 kPa. Both results are reported here because the change was prompted by the comparison. After a short gravity step, the reference node was displaced by 45 mm (S/D = 15 %) with a smooth-step amplitude over 2 s. This time is about 15 times the first vertical period of the sand bed. Loading times of 4 and 6 s gave the same curves within the noise of the solution. Relaxed-stiffness hourglass control was used (Section 4.1). In all production analyses, the kinetic energy stayed below 0.2 % and the artificial energy below 2.6 % of the internal energy.

The model quantities were defined as in the tests. The pressure q is the vertical load divided by the full footing area, less the footing weight of 0.83 kPa, because the load cell was above the footing. The bearing capacity ratio BCR_s is the ratio of reinforced to unreinforced pressure at the same settlement ratio S/D. BCR_t is the same ratio at the same tilt. The model curves were smoothed with a centred moving average over 1 % of S/D. For eccentric loads, the settlement was taken at the footing centre, at the load point and at the edge on the loaded side. The tilt is the difference of the two edge settlements divided by D. The rotation line was computed with the procedure of the source, from the footing profiles at 25, 50, 75 and 100 % of the test ultimate load. The true contact edge was taken as the last node in the plane of the load with a contact pressure above 50 Pa.

4 Verification

4.1 Exact solutions

Table 3 summarises the checks. The elastic stiffness of a smooth rigid circular punch in a large domain differed from the half-space solution by +2.0 %. The same punch in the tank geometry was 18 % stiffer than in a half-space. A modulus back-calculated from these tests with a half-space formula would therefore be too high by a similar amount. For a weightless Tresca material, the rough circular footing gave q/cu = 5.88, against the exact 6.05 [29]. The rough strip footing gave 5.05–5.25, against $2 + \pi = 5.14$. These checks support the representation of

the contact, the rigid footing and the plastic flow at the footing edge. Enhanced hourglass control gave q/c_u = 7.04 for the circular footing, still rising, and was not used.

A weightful frictional soil is a harder test. A rough strip footing on a soil with φ = 30° and ψ = 27° gave 43.0 kPa at S/D = 0.5 %, against the exact 33.9 kPa ($N\gamma$ = 14.75 [30, 31]). With φ = 35° and ψ = 32°, the result was 93.8 kPa against 78.6 kPa. The dilation angles were set 3° below φ for numerical stability; by the reduced-strength relation for non-associated flow [32], the equivalent friction angle then differs from φ by less than 0.1°. The over-prediction of 19–27 % was examined with further analyses (Table 3). It did not change with a mesh of half the element size (43.1 kPa) or with a domain of 3.0 m × 1.5 m (43.1 kPa). A Drucker–Prager material matched to Mohr–Coulomb for associated plane-strain flow gave 43.6 kPa. Modified six-node triangles (CPE6M) gave an excess similar to that of the four-node elements under the same loading rate (51.6 against 48.7 kPa, with a shorter loading time of 0.5 s). The excess therefore does not appear to come from the mesh, the boundaries, the element family or the yield criterion, and its cause was not identified. Implicit finite element analyses with refined triangular meshes have given $N\gamma$ within about 5 % of exact values for associated flow, with collapse loads that decreased as the accuracy increased [33]. The excess found here is therefore larger than is typical of displacement-based finite elements. The higher results with the shorter loading time indicate that the solution is sensitive to the loading rate, so a contribution of residual inertia cannot be excluded. The size of the excess also correlates with the artificial energy, which took 11–30 % of the internal energy in these frictional analyses and about 1 % in the Tresca checks. This correlation does not prove a cause, because the triangles also stored artificial energy. Difficulties of displacement-based elements in $N\gamma$ problems are well known [34–36].

In the production analyses, the dilation angle is small (5°), and artificial energy took only 0.03–1.7 % of each increment of internal energy. The axisymmetric production case with CAX6M elements gave pressures 3–8 % higher than with CAX4R elements up to S/D = 10 %, so the

four-node elements are not stiffer than the triangles in the production setting. Any remaining bias is also absorbed in part by the calibrated friction angle. An excess of 19–27 % in $N\gamma$ corresponds to about 1–1.5° in φ. This is consistent with the calibrated angle of 38° being 1° below the classical estimate (Section 5.1). A bias that depends on the failure mechanism cannot be excluded, and it may contribute to the over-prediction of the eccentric tests (Section 7.3).

Table 3 Verification checks

Check	Model	Reference	Difference
Elastic rigid punch, large domain	3.363×10^6 N/m	3.297×10^6 N/m (half-space)	+2.0 %
Same punch, tank geometry	3.893×10^6 N/m	half-space	+18 % (boundary stiffening)
Tresca, rough circular footing	$q/c_u = 5.88$	6.05 [29]	−2.8 %
Tresca, rough strip footing	$q/c_u = 5.05–5.25$	5.14	−1.8 % to +2.1 %
Weightful strip, φ 30°/ψ 27°, CPE4R	43.0 kPa	33.9 kPa [30]	+27 %
Same, element size −50 % / domain 3.0 m × 1.5 m	43.1 / 43.1 kPa	33.9 kPa	+27 % / +27 %
Same, Drucker–Prager matched for associated plane strain	43.6 kPa	33.9 kPa	+29 %
Same, loading time 0.5 s: CPE4R / CPE6M	48.7 / 51.6 kPa	33.9 kPa	+44 % / +52 %
Weightful strip, φ 35°/ψ 32°, CPE4R	93.8 kPa	78.6 kPa	+19 %
Axisymmetric UR, production parameters, CAX6M vs CAX4R	—	CAX4R	+3 % to +8 % (S/D 1–10 %)
3D vs axisymmetric, elastic	—	—	−0.6 %
3D vs axisymmetric, UR, S/D 1–8 %	—	—	0 to +3.5 %
Axisymmetric UR, element size −25 % / +50 %	—	base mesh	−4.9 to +0.2 % / −1.1 to +2.5 % (S/D ≤ 10 %)
3D, Dg/D 4.5, e/D 0.1875, element size −25 %	—	production mesh	curve ≤ 1.5 %, peak +4.6 %
Larger domain (2.0 m × 1.5 m), UR	—	tank	−5.6 to −10.6 %

4.2 Consistency of the two models

Under central load, the half model and the axisymmetric model agreed within 0.6 % in the elastic range. For the unreinforced sand, the half model gave 0–3.5 % higher pressures at *S/D* = 1–8 % and 4.1–7.8 % at 10–12 %. For the reinforced sand, the comparison revealed a defect of the axisymmetric base mesh. The geonet element next to the axis controlled the stable time

increment. Within the first 0.25 s of loading, its tension jumped to about 5.5 kN/m, and the kinetic energy rose to about 200 times that of the unreinforced analysis. This is a local instability of the explicit integration. It raised BCR_s at S/D = 1 % to 1.36 for D_g/D = 4.5, whereas the half model gave 1.04. On the mesh with element sizes reduced by 25 %, the sand controlled the increment, and the geonet tension at S/D = 1 % was only 0.17–0.18 kN/m. All reinforced axisymmetric results therefore come from this mesh. The defect was not evident from the curves, which looked smooth, or from the kinetic energy, which stayed below 2.7 % of the internal energy. Energy ratios alone may therefore not be a sufficient check for thin, mass-scaled reinforcement in explicit analyses.

5 Central Load: Calibration and Prediction

5.1 Calibration on one test

Only the unreinforced test under central load was used for calibration. The parameters were varied in a grid of φ = 38–40°, ψ = 2–5° and E = 3.5–4.5 MPa, after coarser runs over φ = 35–41°, ψ = 0–8° and E = 2–12 MPa. Each analysis was compared with the test at S/D = 1, 2, 3, 4, 5, 6, 8, 10 and 12 %. Fig. *2b–d* gives the root-mean-square (RMS) error over these points for the final grid. The lowest error, 3.5 %, was found for φ = 38°, ψ = 5° and E = 4 MPa (Fig. 2a). All nine points lie within ±5.2 % of the test. Seven other sets gave errors of 4.8–5.7 %. In these sets, a higher friction angle is balanced by a lower dilation angle or modulus, so the three parameters cannot be identified separately from one curve. The best set was frozen for all further analyses. Four sets of the same error valley were used to show the calibration uncertainty; they form the shaded band in Fig. 2a. The grey line in Fig. 2a is the unsmoothed explicit output, shown to indicate the level of numerical noise. On the finer axisymmetric mesh, the frozen set gives an RMS error of 5.6 %, within the range of the equally good sets.

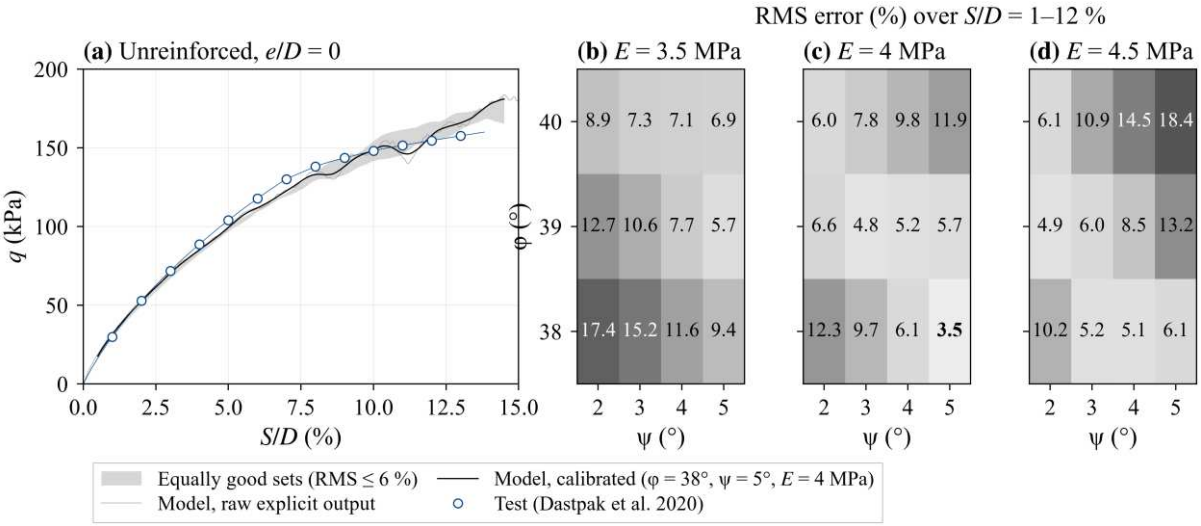

Fig. 2 Calibration on the unreinforced test under central load: (a) load–settlement curves; (b)–(d) RMS error of the parameter grid

The calibrated friction angle of 38° is close to the 39° that the classical bearing capacity equation [37] needs for the measured knee pressure. The dilation angle agrees with $\psi \approx (\varphi - \varphi_{cv})/0.8 = 6°$ [38]. For context, direct shear tests on another uniformly graded silica sand, prepared in the same laboratory, gave $\varphi = 38.2°$ at $D_r = 75$ % [39]. That sand has a different specific gravity (2.71), so the value is not used in this study. The modulus of 4 MPa is low for a dense sand. It is an operative value for a small model test, and it includes the bedding of the footing. The model does not reproduce the change of slope of the test curve at $S/D \approx 7$ %, because a linear elastic, perfectly plastic model has no pre-peak hardening. The model passes below the test curve between $S/D = 3$ % and 8 % and crosses it near 10 %.

5.2 Prediction of the geonet effect

With the frozen parameters, the four reinforced tests under central load were computed without change (Fig. 3). In Fig. 3, the shaded bands show the four equally good parameter sets, and the dashed lines the half model. For $D_g/D = 4.5$, the only reinforced curve published in full, the computed pressure lies between −9.2 % and +4.2 % of the test at $S/D = 1$–12 % (RMS 6.8 %). The bearing capacity ratio at $S/D = 5$ % is 1.22 in the axisymmetric model and 1.23 in the test (−1.2 %). At $S/D = 10$ %, it is 1.45 against 1.46 (−1.0 %). The half model gives 1.18 and 1.40 (−4.2 % in both cases). The four equally good parameter sets give 1.16–1.22 and 1.36–1.53, so

the calibration uncertainty is larger than the difference between the model and the test. An acceptance limit of ±15 % was set before the analyses, and both models meet it.

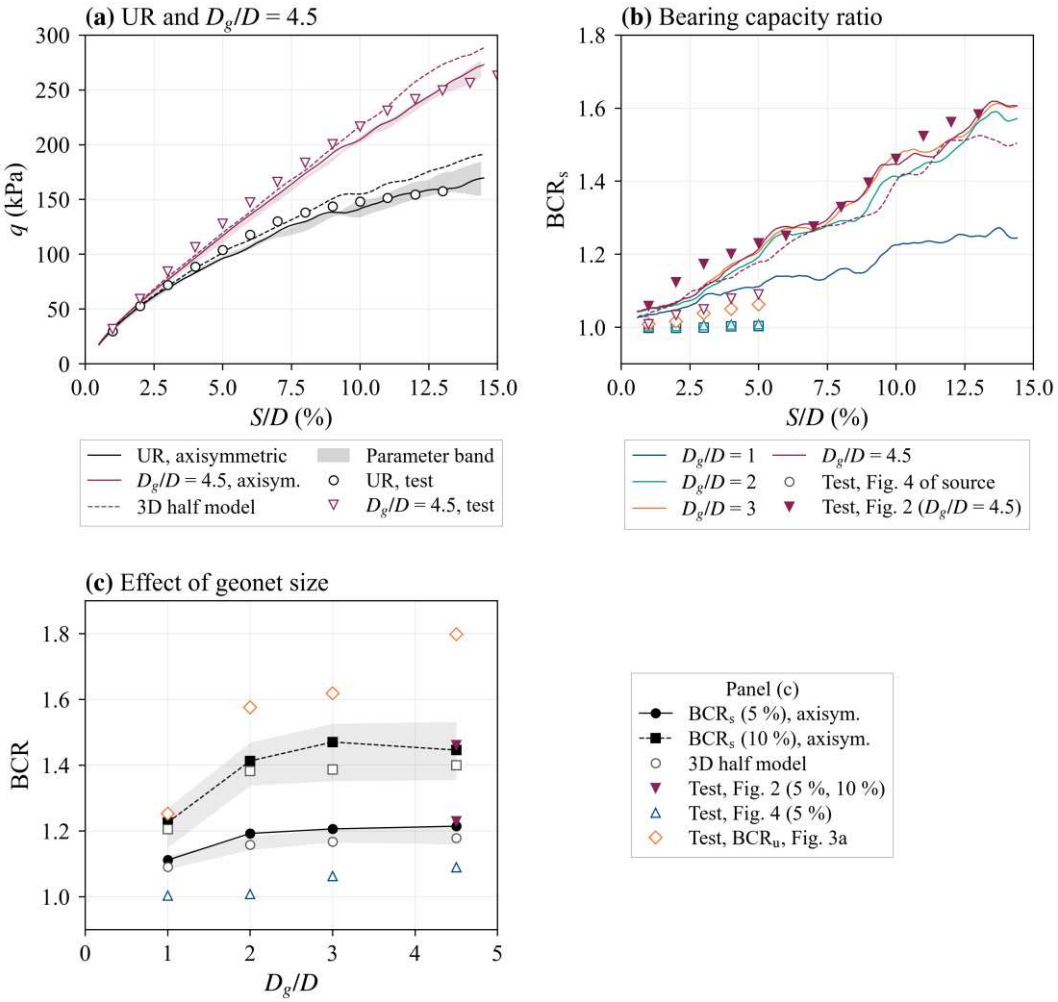

Fig. 3 Central load: (a) load–settlement curves; (b) BCRs against S/D; (c) BCRs against Dg/D

The model also reproduces the effect of geonet size (Fig. 3c). At S/D = 10 %, BCRs rises from 1.23 for D_g/D = 1 to 1.41 for D_g/D = 2, but only to 1.47 and 1.45 for D_g/D = 3 and 4.5. The half model gives 1.21, 1.38, 1.39 and 1.40. The BCR_u values of the source show the same qualitative pattern: a large gain up to D_g/D = 2 and a small gain after that. The small decrease from D_g/D = 3 to 4.5 in the axisymmetric model lies within the noise of the solution. Fig. 3c also shows the BCRu values of the source; they were obtained by tangent intersection with unreported windows and are shown for the trend only. At small settlement, the model gives BCR_s = 1.04–1.06 at S/D = 1 % for all geonet sizes. Fig. 4 of the source gives 1.00–1.01, and the curves of its Fig. 2 give 1.06 (Fig. 3b). The model and the tests therefore agree that the geonet adds little

at small settlement under central load. The geonet tension at S/D = 1 % is only 0.17–0.18 kN/m. This is consistent with the explanation of the source, that the geonet needs some displacement before it is engaged [23]. Between S/D = 3 % and 5 %, the model ratios (1.09–1.22) lie between the two published test sets.

6 Eccentric Load

6.1 Which settlement do the test curves show?

Under central load, all points of the rigid footing settle equally. Under eccentric load, the footing tilts towards the load, and the settlement depends on where it is measured. At half the peak load, the model gives a loaded-edge settlement that is 1.5, 1.9, 2.5 and 4.5 times the centre settlement for e/D = 0.0625, 0.125, 0.1875 and 0.25 (U_R). Practice differs between studies. Badakhshan et al. [12] placed one transducer at the footing centre and one at the load point. Khudhair and Albusoda [14] used the mean of two transducers placed symmetrically about the centre. Rezazadeh Anbarani et al. [40], in the laboratory of the source, plotted the settlement of each side of the footing separately. Dastpak et al. [23] measured the tilt with two transducers on the two sides of the footing, but they did not state which settlement is plotted in their load–settlement curves.

Table 4 gives the RMS error of the model over S/D = 1–12 % for three settlement definitions. With the centre settlement, the errors are 61–148 %. With the load-point settlement, they are 29–65 %. With the loaded-edge settlement, they fall to 7–31 %. This order holds for every eccentricity, with and without the geonet. The mean of the two transducers equals the centre settlement, which gives the poorest agreement. The model therefore suggests that the source plotted the reading of the transducer on the loaded side.

This inference was made after the model results were seen. It was therefore checked with the published data alone. For a rigid footing, the settlement increment at a measuring point x_m is $d_S = d_\theta\,(x_r - x_m)\,D$, where x_r is the rotation line and d_θ the tilt increment. Figs. 2 and 7 of the source therefore give the tilt at each load level, once x_m is chosen. The tilt–load points of the

U_R and $D_g/D = 4.5$ tests then give BCR_t, which can be compared with the tilt plot of the source. With the centre settlement, the implied tilt at the ultimate load reaches 0.6–2.6 rad for $e/D \geq 0.1875$, which is not physically possible. In one case, the rotation line lies between the centre and the loaded edge, so no positive tilt exists. With the load-point settlement, the implied tilt reaches 0.64 rad. With the loaded-edge settlement, it is 0.08–0.32 rad, and the implied BCR_t agrees with the tilt plot of the source within 15 % RMS (about 8 % for tilts of 0.02–0.05 rad). The model tilt at the peak, 0.14–0.31 rad, lies in the same range. The last two rows of Table 4 summarise this check. Of the three readings, the loaded-edge reading is the most consistent with Figs. 2 and 7 and the tilt plot of the source. It is used as the main definition below, and the other two are given in Table 4. Direct confirmation would require the original records.

Table 4 RMS error (%) of the model by settlement definition

Case	e/D	Centre	Load point	Loaded edge
U_R	0	4.4	4.4	4.7
U_R	0.0625	61.2	53.1	22.5
U_R	0.125	68.3	48.3	16.0
U_R	0.1875	109.1	61.8	30.9
U_R	0.25	106.7	29.1	11.0
$D_g/D = 4.5$	0	5.3	5.3	5.3
$D_g/D = 4.5$	0.0625	73.2	65.3	27.1
$D_g/D = 4.5$	0.125	71.1	49.6	11.1
$D_g/D = 4.5$	0.1875	104.2	52.5	12.4
$D_g/D = 4.5$	0.25	148.2	32.4	7.2
Kinematic check: tilt at Q_u implied by the source (rad)		0.11–2.6	0.11–0.64	0.08–0.32
Kinematic check: RMS of implied BCR_t vs the tilt plot of the source (%)		21.0	19.9	15.2

6.2 Load–settlement curves and peak bearing capacity

Fig. 4 compares the test curves (Fig. 2 of the source) with the model curves, which use the loaded-edge settlement. The model follows the general shape of the eccentric test curves, but not their level. The unreinforced pressures are over-predicted, on average by 22, 16, 30 and 4 % for $e/D = 0.0625$, 0.125, 0.1875 and 0.25. For $D_g/D = 4.5$, the mean errors are +26, +7, +9

and −4 %. For e/D = 0.125 and 0.1875, the reinforced curves are matched within 3 % up to S/D = 3 %, and the error grows to about 22 % at S/D = 12 %. For e/D = 0.25, the model is 6–13 % low up to S/D = 5 %. The test curves of D_g/D = 4.5 rise without a peak up to S/D = 18–23 %. The unreinforced curves outside the kern show a peak, as in the model.

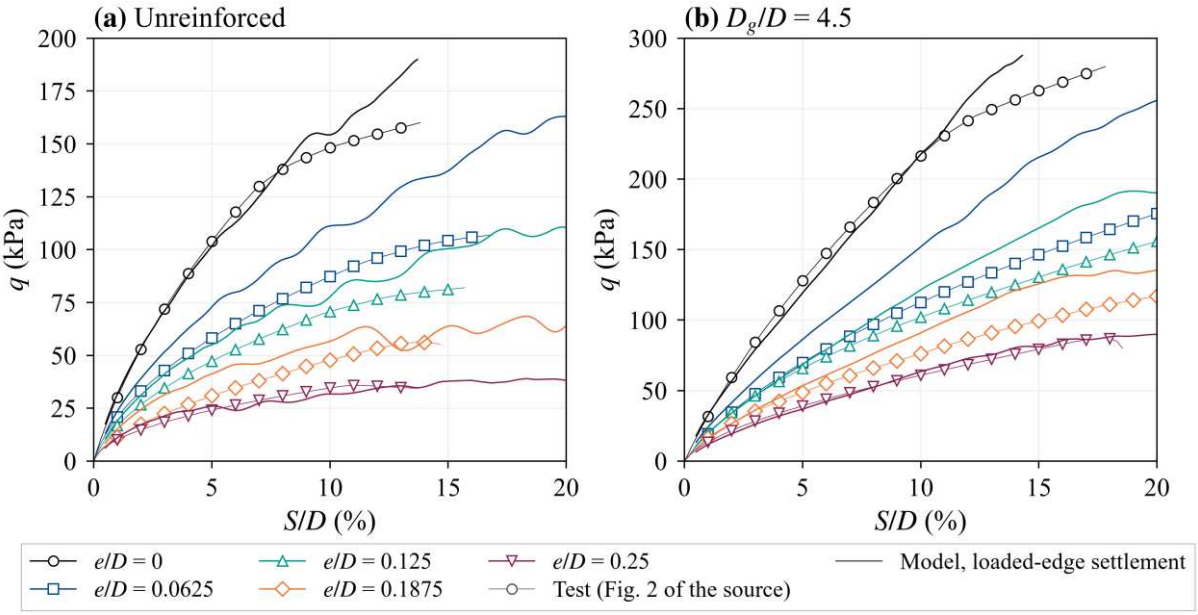

Fig. 4 Load–settlement curves under eccentric load: (a) unreinforced; (b) Dg/D = 4.5

Outside the kern, the peak pressure is a load, so it does not depend on the settlement definition. The model over-predicts the unreinforced peaks by 23 % (69.2 vs 56.1 kPa, e/D = 0.1875) and 12 % (40.0 vs 35.8 kPa, e/D = 0.25). The peak-based bearing capacity ratio BCR_u, however, agrees well with the tests for all four geonet sizes (Fig. 5b). At e/D = 0.1875, the model gives 1.35, 1.84, 2.00 and 2.01 for D_g/D = 1, 2, 3 and 4.5. The tests give 1.39, 1.94, 2.05 and 2.16. At e/D = 0.25, the model gives 1.34, 2.13, 2.31 and 2.29, against 1.39, 2.04, 2.28 and 2.47. All differences lie between −7.3 % and +4.2 %. The model also reproduces the main trend of the source: BCRu outside the kern increases with eccentricity, and it hardly grows beyond D_g/D = 2–3. Part of this agreement comes from the ratio itself, because the reinforced peaks are also over-predicted, by 15 % and 4 %. The short bars in Fig. 5b show the peaks with geonet rupture (Section 7.3).

6.3 Bearing capacity ratio at small settlement and tilt

At small deformation, the agreement is poorer (Fig. 5a, c). Fig. 5a compares *BCRs* for D_g/D = 4.5 at S/D = 1 % and 5 % with Fig. 4 of the source. With the loaded-edge settlement, the model BCR_s at S/D = 5 % rises from 1.17 (e/D = 0) to 1.18, 1.25, 1.30 and 1.42. Fig. 4 of the source gives 1.09, 1.20, 1.38, 1.45 and 1.63. The model therefore reproduces the increase with eccentricity, but it under-predicts the benefit by 10–13 % for $e/D \geq 0.125$. At S/D = 1 %, the model gives 1.02–1.06 for all eccentricities and geonet sizes, whereas the tests give 1.06–1.37 for $e/D \geq 0.125$. The comparison by tilt (Fig. 5c, tests from the tilt plot of the source) shows the same gap. At a tilt of 0.01 rad, the model BCR_t is 1.02–1.05, against 1.21–1.59 in the tests for D_g/D = 4.5. At 0.05 rad, the model gives 1.23–1.42, against 1.25–1.57. Only for e/D = 0.0625 does the model reach the test value at larger tilt. BCR_t does not depend on the settlement definition, so this gap reflects a limitation of the model rather than of the settlement definition.

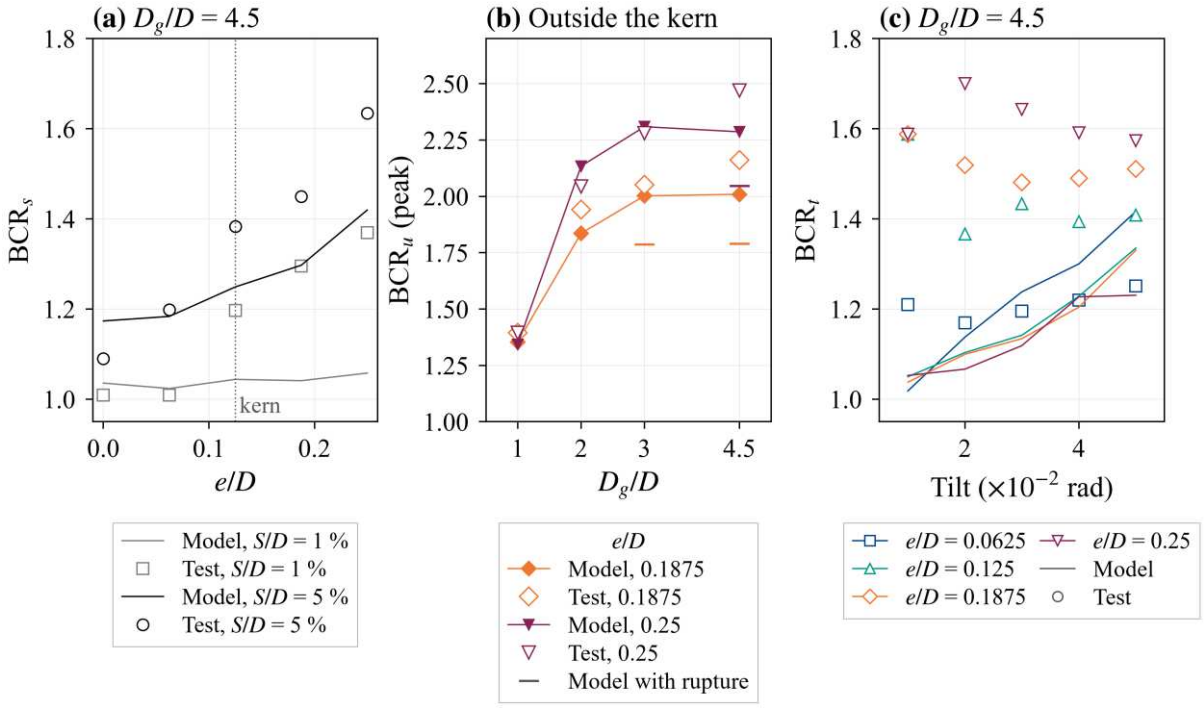

Fig. 5 Geonet benefit under eccentric load: (a) BCRs against e/D; (b) peak BCRu against Dg/D; (c) BCRt against tilt

The gap comes mainly from the unreinforced tests. At S/D = 1 %, the model over-predicts the unreinforced pressures by 10–33 % for $e/D \geq 0.0625$. For $e/D \geq 0.125$, it gives reinforced

pressures 1–13 % below the tests. The unreinforced footing under eccentric load is therefore softer in the tests than in the model. Possible reasons are discussed in Section 7.3.

6.4 Rotation line and loss of contact

Fig. 6 compares the rotation line of the tests (Fig. 7 of the source) with the rotation line and the true contact edge of the model. The model rotation line was computed with the procedure of the source at the same absolute loads as the tests. Here x is measured from the loaded edge. The model rotation line follows the trend of the tests: it moves towards the loaded edge as the load increases and as the eccentricity grows. The true contact edge behaves differently. It lies at $x/D \approx 0.97$ for $e/D = 0.0625$, 0.79–0.91 for 0.125, 0.70–0.73 for 0.1875 and 0.50–0.54 for 0.25. It hardly changes with the load or with the geonet. For $e/D \geq 0.125$, the rotation line lies 0.08–0.23 D outside the true contact edge, and it moves with the load while the contact edge does not.

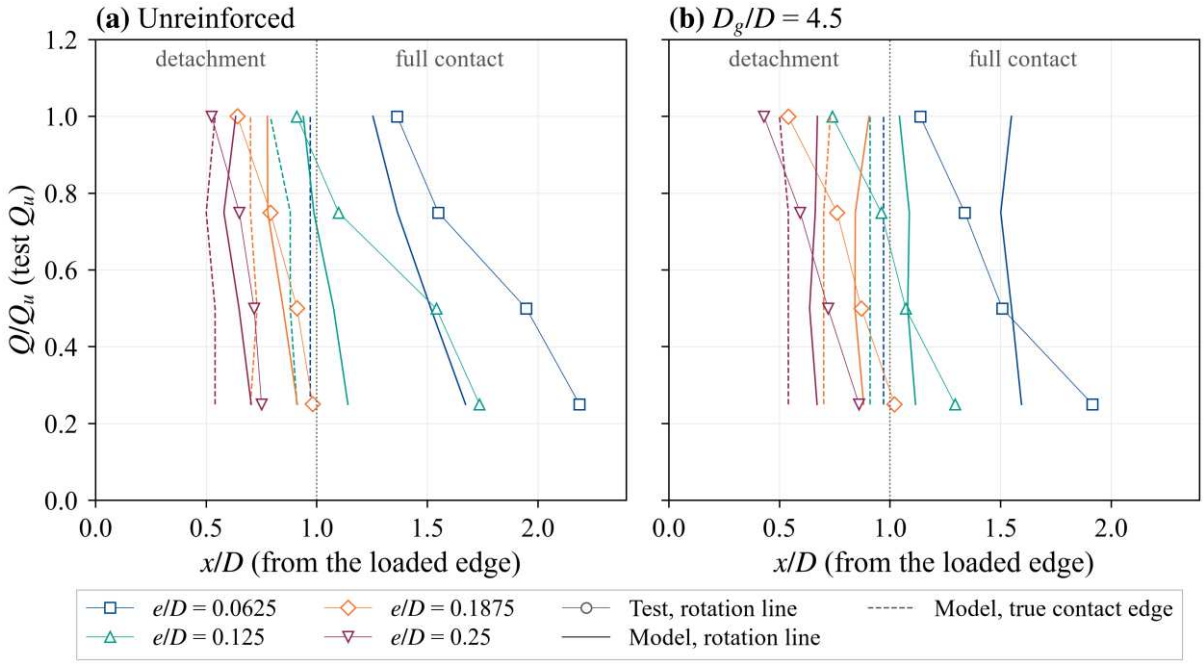

Fig. 6 Rotation line and contact edge against load level: (a) unreinforced; (b) Dg/D = 4.5

The difference can be explained kinematically. The rotation line is the point of zero incremental settlement between two load levels. Its position is set by the ratio of incremental settlement to incremental tilt. This ratio changes as the plastic zone under the loaded edge grows. A moving rotation line therefore does not by itself indicate a moving contact edge. In the model, the

contact width is set mainly by the eccentricity. For strip footings at collapse, finite element analyses have shown detachment for $e/B > 1/6$ and a contact pressure distribution of the same shape relative to the effective width $B - 2e$ [33]. A contact width governed by the eccentricity is consistent with these results. The source concluded that detachment occurs even on the kern boundary at high load. The model indicates a small loss of contact at $e/D = 0.125$, of 0.1–0.2 D, but at all load levels. This value is sensitive to the pressure threshold, because the pressure near the back edge is small on the kern boundary. For $e/D = 0.25$, the true contact covers about half of the diameter. This agrees with the source, which inferred that about half the diameter detaches at failure [23].

7 Discussion

7.1 Why does the geonet benefit grow with eccentricity?

The model offers an explanation at the ultimate state, where it agrees with the tests. Outside the kern, the absolute gain from the geonet changes little with eccentricity. For $D_g/D = 4.5$, the model gain is 69.9 kPa at $e/D = 0.1875$ and 51.4 kPa at $e/D = 0.25$. The tests give 65.1 and 51.9 kPa. The unreinforced capacity falls much faster, from 69.2 to 40.0 kPa in the model and from 56.1 to 35.8 kPa in the tests. A similar gain is then a larger fraction of a smaller unreinforced capacity, so BCR_u rises.

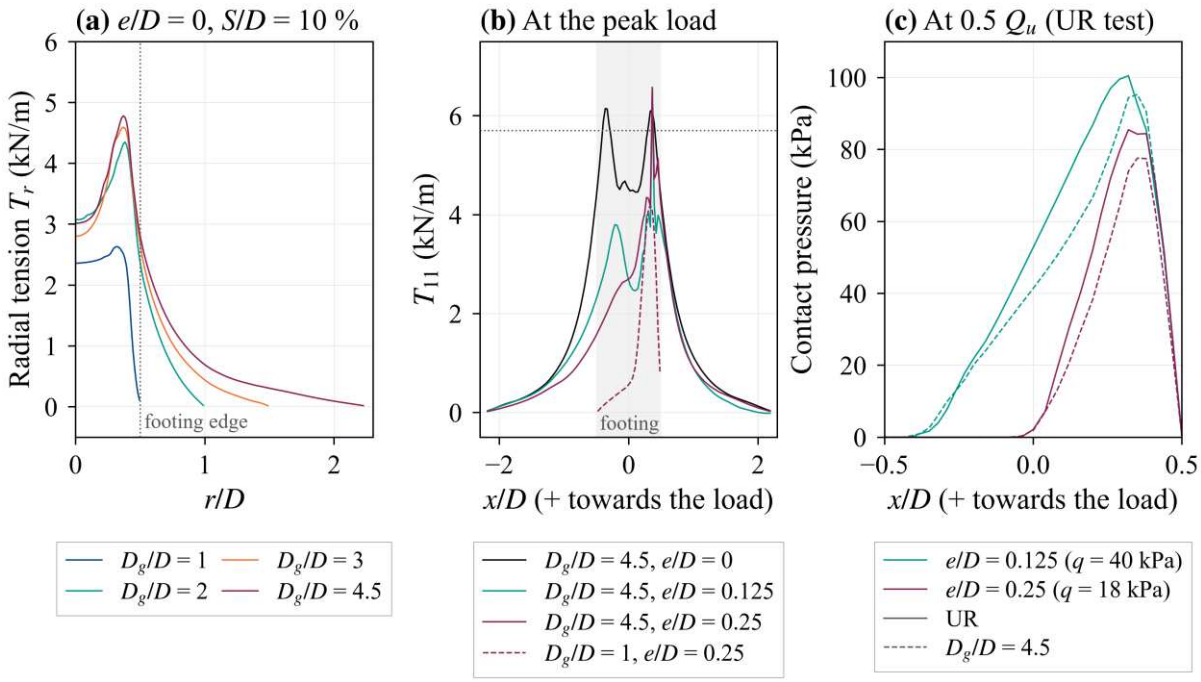

Fig. 7 Geonet tension and contact pressure in the models: (a) radial tension under central load; (b) tension along the plane of the load; (c) contact pressure

The geonet tension indicates why the gain is maintained. Fig. 7b shows the tension along the plane of the load at the peak load of the half model; for $e/D = 0$, it is taken at the end of the analysis ($S/D = 15$ %). The dotted line marks the tensile strength of 5.7 kN/m. Under eccentric load, the deformation concentrates below the loaded half of the footing. The geonet tension has its maximum at $x/D \approx +0.36$ from the centre, below the loaded half. At the peak, it is 3.6–4.8 kN/m there for $D_g/D = 4.5$ and $e/D \geq 0.125$, that is, 63–84 % of the strength. The narrow maxima in Fig. 7b are single elements in which the strain localises after the membrane reaches its limit. The geonet is therefore strongly mobilised, even when the unreinforced mechanism becomes small and shallow. The unreinforced footing, in contrast, loses capacity for two reasons. Its contact width shrinks to about $D/2$ at $e/D = 0.25$ (Section 6.4), and its failure wedge forms on one side only. Fig. 7c shows this loss of contact in the contact pressure, at 50 % of the test ultimate load of the unreinforced footing. The geonet at $u/D = 0.17$ crosses the shallow wedge below the loaded edge. It may force the mechanism to mobilise more soil than in the unreinforced case. Under central load, the tension spreads over the whole footing width at a

lower level; at S/D = 10 %, its maximum is 4.8 kN/m. This is consistent with the lower BCR_u under central load.

Badakhshan and Noorzad [10] found the opposite trend outside the kern. Their footing was 2.5 times smaller, and they used several geogrid layers at different depths. The source attributed the difference to scale [23]. The present results suggest one further possible factor: whether the reinforcement crosses the shallow one-sided wedge of the eccentric footing. Reinforcement placed deeper, or a footing with a deeper mechanism, may not benefit in the same way. This cannot be tested with the present data.

7.2 Why does a geonet wider than 2D add little?

Fig. 7a shows the radial geonet tension of the axisymmetric model under central load at S/D = 10 %. The tension has its maximum at $r \approx 0.11$ m, below the footing. It is 2.6, 4.4, 4.6 and 4.8 kN/m for D_g/D = 1, 2, 3 and 4.5. For D_g/D = 4.5, the tension at the footing edge is 2.8 kN/m. At $r = D$, it is only 0.7 kN/m, or 14 % of the maximum. A geonet of D_g/D = 1 ends at the footing edge, where the longer geonet still carries 59 % of its maximum tension. The short geonet must lose this tension at its free edge, so its maximum is lower and its benefit smaller. Beyond $r = D$, the sand moves little relative to the geonet, so the geonet carries little tension there. Extending the geonet beyond D_g/D = 2 therefore adds mainly a lightly loaded outer ring. The same holds under eccentric load. At the peak, the tension at $x = \pm D$ is 7–20 % of the maximum for D_g/D = 3 and 4.5. For D_g/D = 1, the peak tension stays at 3.7–4.2 kN/m with strains below 2 %, whereas the larger geonets reach the membrane limit below the loaded half. This is consistent with the small BCR_u of D_g/D = 1 at all eccentricities. The source explained the plateau by sufficient anchorage beyond D_g/D = 2 [23]. The model supports this, with one refinement: the geonet cannot slip in the model, so the plateau here results from the extent of the tension zone, not from pull-out. For strip footings, longer reinforcement, up to four to five times the footing width, has been reported to be effective (as summarised in [23]). One possible

reason is that the tension in a circular membrane decays faster with distance than in a plane-strain sheet.

7.3 Limitations

The settlement definition of the eccentric tests is inferred, not reported. The model and the kinematic check agree on the loaded edge, but direct confirmation would need the original records.

The model over-predicts the unreinforced eccentric response (mean +4 % to +30 % with the loaded-edge settlement), and it under-predicts the geonet benefit at small tilt. The sand model has a uniform modulus and no pre-failure plasticity. Elastic–perfectly plastic analyses are best suited to problems in which the pre-failure non-linearity is small [33]. Under eccentric load, the deformation concentrates in the shallow sand below the loaded edge, where the stress is low. A sensitivity analysis tested the effect of the stress level. The modulus was made to increase with depth, $E = Es\ \sqrt{(z/0.15\ \text{m})}$, and E_s = 4.25 MPa was recalibrated on the same central test. The errors at S/D = 1–4 % were then +4.8 % to −1.3 %, similar to the production set. With this modulus, the mean error of the unreinforced eccentric tests fell from +22 % to +17 % (e/D = 0.0625) and from +30 % to +19 % (e/D = 0.1875). At S/D = 1 %, it fell from +13.5 % to +4.5 % and from +33 % to +13 %. However, the reinforced curves softened by a similar amount, so BCR_s and BCR_t hardly changed. For e/D = 0.1875, BCR_t at 0.01 rad was 1.05, against 1.59 in the test. Stress-dependent stiffness thus explains part of the unreinforced over-prediction, but not the early geonet benefit. That benefit may come from mechanisms that the model does not contain, such as the strain-dependent stiffness of sand, the confinement of sand within the geonet apertures and the seating of the footing at small load. The hardening soil model with small-strain stiffness [41] has been used to predict chamber footing tests from triaxial-derived parameters, with bearing stresses within about 20 % at s/D = 0.5–1 % in most cases [22]. Such a model requires triaxial data, which are not available for the sand of the source. It is recommended for future work on this problem.

The geonet strain exceeded the rupture strain of 9 % before the peak in 7 of the 20 reinforced eccentric cases. The strain localised in one element below the loaded half, as expected for a non-hardening membrane. Analyses with geonet rupture (ductile damage and element deletion at 9 % strain) gave identical curves up to rupture and peaks lower by 10.5–14.8 %. Rupture occurred beyond a loaded-edge settlement of 12 %, so the compared curves were not affected. The tests of $D_g/D = 4.5$ show no sudden drop up to S/D = 18–23 %. The test end pressures for $e/D = 0.25$ (87.7 kPa) and 0.1875 (121.2 kPa) lie between or close to the two model bounds (81.9–91.4 and 123.9–139.1 kPa). The perfect bond also tends to concentrate the geonet strain, and slip would reduce it.

The von Mises geonet allows a principal tension up to 15 % above the uniaxial strength under biaxial tension. The tank makes the elastic response 18 % stiffer than a half-space, and a larger domain lowered the unreinforced pressures by 6–11 %. The results are therefore specific to the test geometry. Finally, the weightful frictional benchmark was over-predicted by 19–27 % with both element families and both yield criteria. Its cause was not fully resolved (Section 4.1). It affects strongly dilatant flow far more than the production analyses, but a small, mechanism-dependent bias cannot be excluded.

8 Conclusions

The 25 model tests of Dastpak et al. [23] were back-analysed with axisymmetric and three-dimensional Abaqus/Explicit models. The sand was calibrated on one test, and the other 24 tests were computed without further adjustment. The main conclusions are as follows.

Under central load, the computed bearing capacity ratio of the largest geonet was within 1.2 % (axisymmetric) and 4.2 % (3D) of the test at S/D = 5 % and 10 %. The calibration uncertainty, 1.16–1.22 at 5 %, was larger than this difference. The model reproduced the small geonet benefit at small settlement and the plateau beyond $D_g/D = 2$.

The settlement definition had a strong effect on the comparison of the eccentric tests. The loaded-edge settlement gave RMS errors of 7–31 %, against 61–148 % for the centre. A

kinematic check of the published curves, rotation lines and BCR_t values supports this reading independently of the model. Reports of eccentric footing tests would benefit from stating where the plotted settlement is measured.

Outside the kern, the peak-based BCRu was reproduced within −7.3 % to +4.2 % for all geonet sizes. In the model, it rises with eccentricity because the geonet remains strongly mobilised below the loaded half, while the unreinforced capacity falls with the contact width.

Most geonet tension developed within one footing diameter of the centre. This is consistent with the small additional benefit of a geonet wider than 2D.

The rotation line from two transducers lay 0.08–0.23 *D* outside the computed contact edge, and it moved with load while the contact edge did not. It is therefore better regarded as a kinematic quantity than as a measure of the contact area.

The model over-predicted the unreinforced eccentric pressures and under-predicted the early benefit of the geonet. A modulus that increases with depth reduced the first error by about one quarter to one third but did not change the second. The early geonet benefit under eccentric load was not reproduced by the present model.

References

1. Meyerhof GG (1953) The bearing capacity of foundations under eccentric and inclined loads. In: Proceedings of the 3rd International Conference on Soil Mechanics and Foundation Engineering, Zurich, vol 1, pp 440–445

2. Highter WH, Anders JC (1985) Dimensioning footings subjected to eccentric loads. J Geotech Eng 111(5):659–665. https://doi.org/10.1061/(ASCE)0733-9410(1985)111:5(659)

3. Binquet J, Lee KL (1975) Bearing capacity tests on reinforced earth slabs. J Geotech Eng Div 101(12):1241–1255. https://doi.org/10.1061/AJGEB6.0000219

4. Yetimoglu T, Wu JTH, Saglamer A (1994) Bearing capacity of rectangular footings on geogrid-reinforced sand. J Geotech Eng 120(12):2083–2099. https://doi.org/10.1061/(ASCE)0733-9410(1994)120:12(2083)

534 5. Michalowski RL (2004) Limit loads on reinforced foundation soils. J Geotech Geoenviron
535 Eng 130(4):381–390. https://doi.org/10.1061/(ASCE)1090-0241(2004)130:4(381)
536 6. Abu-Farsakh M, Chen Q, Sharma R (2013) An experimental evaluation of the behavior of
537 footings on geosynthetic-reinforced sand. Soils Found 53(2):335–348.
538 https://doi.org/10.1016/j.sandf.2013.01.001
539 7. Patra CR, Das BM, Bhoi M, Shin EC (2006) Eccentrically loaded strip foundation on
540 geogrid-reinforced sand. Geotext Geomembr 24(4):254–259.
541 https://doi.org/10.1016/j.geotexmem.2005.12.001
542 8. El Sawwaf M (2009) Experimental and numerical study of eccentrically loaded strip footings
543 resting on reinforced sand. J Geotech Geoenviron Eng 135(10):1509–1518.
544 https://doi.org/10.1061/(ASCE)GT.1943-5606.0000093
545 9. Demirdöğen S, Gürbüz A, Yünkül K (2024) Performance of eccentrically loaded strip
546 footings on geocell-reinforced soil. Geotext Geomembr 52(4):421–434.
547 https://doi.org/10.1016/j.geotexmem.2023.12.007
548 10. Badakhshan E, Noorzad A (2015) Load eccentricity effects on behavior of circular footings
549 reinforced with geogrid sheets. J Rock Mech Geotech Eng 7(6):691–699.
550 https://doi.org/10.1016/j.jrmge.2015.08.006
551 11. Badakhshan E, Noorzad A (2017) Effect of footing shape and load eccentricity on behavior
552 of geosynthetic reinforced sand bed. Geotext Geomembr 45(2):58–67.
553 https://doi.org/10.1016/j.geotexmem.2016.11.007
554 12. Badakhshan E, Noorzad A, Zameni S (2020) Eccentrical behavior of square and circular
555 footings resting on geogrid-reinforced sand. Int J Geotech Eng 14(2):151–161.
556 https://doi.org/10.1080/19386362.2018.1425197
557 13. Basha AM, Eldisouky EA (2023) Effect of eccentric loads on the behavior of circular
558 footing with/without skirts resting on sand soil. Int J Geo-Eng 14:13.
559 https://doi.org/10.1186/s40703-023-00192-z

14. Khudhair RR, Albusoda BS (2025) A comparative experimental study of circular footings on sand reinforced with geogrid and loosely skirted foundations under eccentric loading. Eng Technol Appl Sci Res 15(5):27227–27236. https://doi.org/10.48084/etasr.12535

15. Fathipour H, Payan M (2023) Seismic bearing capacity of eccentrically and obliquely loaded strip footings on geosynthetic-reinforced soil. Int J Geomech 23(6):04023057. https://doi.org/10.1061/IJGNAI.GMENG-8316

16. Keawsawasvong S, Fathipour H, Zanganeh Ranjbar P, Payan M, Jamsawang P (2024) Influence of soil fabric anisotropy on the bearing capacity of geosynthetic-reinforced foundations under eccentric and inclined loadings. Soils Found 64(3):101479. https://doi.org/10.1016/j.sandf.2024.101479

17. Yaghoobi B, Fathipour H, Payan M, Jamshidi Chenari R (2024) Bearing capacity of footings on geosynthetic-reinforced soils under combined loading. Geosynth Int 31(5):568–596. https://doi.org/10.1680/jgein.22.00385

18. Du D, Xu J, Gong W, Dias D (2024) Kinematic bearing capacity analysis of strip footings on reinforced soils using discretisation technique. Eur J Environ Civ Eng 28(16):3945–3964. https://doi.org/10.1080/19648189.2024.2401149

19. Das PP, Khatri VN, Lai VQ, Keawsawasvong S (2023) Bearing capacity estimation of ring footing on layered sand with geogrid at the interface using FELA and MARS. Int J Geosynth Ground Eng 9(5):57. https://doi.org/10.1007/s40891-023-00475-6

20. Boushehrian JH, Hataf N (2003) Experimental and numerical investigation of the bearing capacity of model circular and ring footings on reinforced sand. Geotext Geomembr 21(4):241–256. https://doi.org/10.1016/S0266-1144(03)00029-3

21. Tabaroei A, Zhao Y, Pham TA (2026) Settlement and mobilized bearing capacity of circular footings on geosynthetic-reinforced sand: experimental and numerical study. Geotech Geol Eng 44(4):197. https://doi.org/10.1007/s10706-026-03677-7

585 22. Bagbag AA, Lehane BM, Doherty JP (2017) Predictions of footing and pressuremeter
586 response in sand using a hardening soil model. Proc Inst Civ Eng Geotech Eng 170(6):479–
587 492. https://doi.org/10.1680/jgeen.17.00040
588 23. Dastpak P, Abrishami S, Sharifi S, Tabaroei A (2020) Experimental study on the behavior
589 of eccentrically loaded circular footing model resting on reinforced sand. Geotext Geomembr
590 48(5):647–654. https://doi.org/10.1016/j.geotexmem.2020.03.009
591 24. Lambe TW (1973) Predictions in soil engineering. Géotechnique 23(2):151–202.
592 https://doi.org/10.1680/geot.1973.23.2.151
593 25. Tabaroei A, Abrishami S, Hosseininia ES (2017) Comparison between two different
594 pluviation setups of sand specimens. J Mater Civ Eng 29(10):04017157.
595 https://doi.org/10.1061/(ASCE)MT.1943-5533.0001985
596 26. Dastpak P, Abrishami S, Rezazadeh Anbarani M, Dastpak A (2021) Effect of perforated
597 plates on the relative density of uniformly graded reconstituted sands using air pluviation
598 method. Transp Infrastruct Geotechnol 8(4):569–589. https://doi.org/10.1007/s40515-021-
599 00150-1
600 27. Tabaroei A, Abrishami S, Seyedi Hosseininia E, Ganjian N (2018) A study on bearing
601 capacity of circular footing resting on geogrid reinforced granular soil. Amirkabir J Civ Eng
602 50(5):973–986 (in Persian, with English abstract).
603 https://doi.org/10.22060/ceej.2017.13150.5339
604 28. Briaud JL, Jeanjean P (1994) Load settlement curve method for spread footings on sand.
605 In: Vertical and horizontal deformations of foundations and embankments. Geotechnical
606 Special Publication 40, ASCE, New York, pp 1774–1804
607 29. Eason G, Shield RT (1960) The plastic indentation of a semi-infinite solid by a perfectly
608 rough circular punch. Z Angew Math Phys 11(1):33–43. https://doi.org/10.1007/BF01591800

609 30. Martin CM (2005) Exact bearing capacity calculations using the method of characteristics.
610 In: Barla G, Barla M (eds) Proceedings of the 11th International Conference of IACMAG,
611 Turin, vol 4, pp 441–450
612 31. Hjiaj M, Lyamin AV, Sloan SW (2005) Numerical limit analysis solutions for the bearing
613 capacity factor Nγ. Int J Solids Struct 42(5–6):1681–1704.
614 https://doi.org/10.1016/j.ijsolstr.2004.08.002
615 32. Drescher A, Detournay E (1993) Limit load in translational failure mechanisms for
616 associative and non-associative materials. Géotechnique 43(3):443–456.
617 https://doi.org/10.1680/geot.1993.43.3.443
618 33. Loukidis D, Chakraborty T, Salgado R (2008) Bearing capacity of strip footings on purely
619 frictional soil under eccentric and inclined loads. Can Geotech J 45(6):768–787.
620 https://doi.org/10.1139/T08-015
621 34. Frydman S, Burd HJ (1997) Numerical studies of bearing-capacity factor Nγ. J Geotech
622 Geoenviron Eng 123(1):20–29. https://doi.org/10.1061/(ASCE)1090-0241(1997)123:1(20)
623 35. Erickson HL, Drescher A (2002) Bearing capacity of circular footings. J Geotech
624 Geoenviron Eng 128(1):38–43. https://doi.org/10.1061/(ASCE)1090-0241(2002)128:1(38)
625 36. Loukidis D, Salgado R (2009) Bearing capacity of strip and circular footings in sand using
626 finite elements. Comput Geotech 36(5):871–879.
627 https://doi.org/10.1016/j.compgeo.2009.01.012
628 37. Vesić AS (1973) Analysis of ultimate loads of shallow foundations. J Soil Mech Found Div
629 99(1):45–73. https://doi.org/10.1061/JSFEAQ.0001846
630 38. Bolton MD (1986) The strength and dilatancy of sands. Géotechnique 36(1):65–78.
631 https://doi.org/10.1680/geot.1986.36.1.65
632 39. Rezazadeh Anbarani M, Abrishami S, Bayat M (2023) Effect of geogrid reinforcement and
633 soil relative density on performance and contact pressures of ring foundations on sand. KSCE
634 J Civ Eng 27(12):5135–5148. https://doi.org/10.1007/s12205-023-1080-2

635 40. Rezazadeh Anbarani M, Abrishami S, Bayat M (2024) Influence of load eccentricity on
636 performance and contact pressures of ring foundations on geogrid-reinforced sand. KSCE J
637 Civ Eng 28(12):5524–5533. https://doi.org/10.1007/s12205-024-2307-6
638 41. Schanz T, Vermeer PA, Bonnier PG (1999) The hardening soil model: formulation and
639 verification. In: Brinkgreve RBJ (ed) Beyond 2000 in computational geotechnics: 10 years of
640 PLAXIS International. Balkema, Rotterdam, pp 281–296